nature communications

Article

https://doi.org/10.1038/s41467-025-61261-8

# A skin-interfaced three-dimensional closed-loop sensing and therapeutic electronic wound bandage

Received: 29 November 2024

Accepted: 18 June 2025

Published online: 01 July 2025

Check for updates

Xingcan Huang[1,20], Qiang Zhang[1,2,20], Yawen Yang[1,20], Lung Chow[1,20], Jie Ma[3,20], Guoqiang Xu[1], Fang Guo[4,5], Xinxin He[1], Zhiyuan Li[1], Guangyao Zhao[1], Jingyou Su[6], Guihuan Guo[1], Jiachen Wang[1], Yanli Jiao[1,7], Zhan Gao[1], Jiyu Li[1,8], Jingkun Zhou[1,7], Chun Ki Yiu[1,7], Jian Li[1,7], Yi Chen[9,10,11], Pengcheng Wu[1], Kuanming Yao[1], Yiming Liu[1,12], Dengfeng Li[1], Binbin Zhang[1,7], Hongwei Chu[1], Yue Hu[1,13], Ya Huang[1,14], Zhenlin Chen[1,7], Kangning Ren[6], Bo Fang[15,16], Rungong Yang[17] ✉, Heng Li[3,15] ✉, Xiaoming Tao[15,16] ✉, Xiaohui Ma[18] ✉ & Xinge Yu[1,2,7,19] ✉

Chronic wound healing is a complex and long-standing problem, that has been a major and critical clinical concern around the world for years. Recent advances in digital wound dressings open new possibilities for solving the problem. Here, we report a battery-free, fully permeable, skin-adhesive, stretchable electronic wound bandage (iSAFE) for intelligent wound management. This electronic bandage exhibits superior properties in multiple features and can be conformally adhered to the skin wound. In addition, the iSAFE can accurately assess the wound conditions in-situ and thus adaptively perform localized drug release. The results from both in vitro and in vivo studies on animals prove the validity of wound monitoring, wound healing boosting and intelligent closed-loop wound management. Clinical trials on patients across age 18 to 95 with various types of wounds are performed. These results all indicate the unique and universality of the reported technology for wound monitoring and management.

Recent advances of materials and devices in soft electronics have significantly boosted the technological revolution in many fields, i.e., healthcare monitoring[1–5], human-machine interface[6,7], haptic feedback[8–10] et al. It is believed that soft electronics will be the key for future healthcare monitoring, as it can provide continuous and long-term health signal assessment, that is especially important for people with chronic diseases[4,5,11]. One grand challenge in long term healthcare management is chronic wound management, which associates with many factors (e.g., diabetic induced ulcers, nonhealing surgical incisions, and venous ulceration) and significantly increases unbearable pain for patients and huge financial burdens[12–14]. Wound healing goes through several phases, including hemostasis, inflammation, proliferation and remodeling. Each phase need to be carefully managed, as various environmental and physiological factors could influence the process[15–17]. Typically, these factors and the state of wound healing can be inferred from the dynamic changes in wound exudates. For example, wound healing is accompanied by a reduction in exudate pH levels from alkaline to neutral, and a rise in the skin temperature around an acute wound during the initial days post-infection[18–20]. Monitoring glucose concentration in the wound is another important issue, which facilitates the regulation of blood glucose in diabetic patients and reflects wound status, thereby reducing infection risks[21,22]. Timely sensing these signals with necessary interventions is extremely important for intelligent wound healing, monitoring and management, however, the current

A full list of affiliations appears at the end of the paper. ✉e-mail: yangrungong@139.com; heng.li@polyu.edu.hk; xiao-ming.tao@polyu.edu.hk; maxiaohui@301hospital.com.cn; xingeyu@cityu.edu.hk

technologies can't meet the requirements for those purposes. Therefore, it's very urgent to develop new wound management technologies to continuously monitor multiple physical/chemical/bio markers with closed-loop management systems.

Two foundations of such intelligent technologies are associated with bioactive materials that can sense related physical/chemical/bio markers during wound healing, and digital sensing wound platforms that exhibit capabilities of data collection, analysis and intervention. The current works on either bioactive materials or digital sensing platforms are still in the early stages, as they solely focus on materials biofunctions or electronic properties. How to integrate the digital sensing platform with a clinical standard wound dressing into a real practical wound management system is still a hurdle. Key issues, from use comfortability to bio-adhesiveness, to anti-bacterial properties, to real-time accurate wound digital monitoring, and to high-level integration strategies need to be addressed, so the system can allow to in-situ monitor wound conditions and adaptively provide timely and reliable analysis, enabling integrative diagnosis and personalized treatment. To sum up, there still are huge gaps for achieving the ideal intelligent electronic wound bandage, including but not limited to (1) ideal wound dressing materials, (2) dynamic and intelligent wound monitoring and management and (3) the combination of biomaterials and bioelectronics, permeable electronics and encapsulation (Supplementary Fig. 1).

To this end, we report a battery-free, skin-adhesive, permeable, moisturizing, waterproof, intelligent, stretchable, antibacterial and multifunctional electronics (iSAFE), focusing on integral perspectives of the bioactive electronic-wound interface (BEWI), sensing, localized adaptive drug delivery, as well as the dynamic integration between electronics and biomaterials. The iSAFE is ultrathin and stretchable with a similar thickness to the epidermis and excellent skin-adhesion, capable of conforming to skin deformation. The iSAFE not only shows similar functions as human skin in terms of permeability, stretchability, and adaptability, but also encompasses properties including antibacterial ability, hemostasis, water retention, permeability and pro-healing. Apart from its passive biofunctions of promoting wound healing, managing moisture levels, and providing a protective barrier against external contaminants, the BEWI is an active participant with electrical stability and the ability to selectively carry and release medications by interacting with the intelligent control circuits in the wound management system. Combining with biosensors and near-field communication (NFC) technology, the battery-free iSAFE is able to achieve in-situ continuous assessment of wound status and the on-demand drug release, effectively managing diverse wound complications in a timely manner. More importantly, the clinical trials of 10 patients across age 18 to 95 with various types of chronic and acute wounds were conducted, and the results exhibit great accuracy for assessing wound conditions and directing personalized wound treatment. Benefitting from the advanced design and integration strategies, the iSAFE perfectly bridges the gap between the realm of dynamic tissue properties and electronics, orchestrates bioactive interface, biosensors, and bioelectronics, and solves the seemingly contradictory demands of permeability and waterproofness, opening up new possibilities for intelligent wound management (Supplementary Note 1).

## Results

### Design of the battery-free, skin-adhesive iSAFE system

The iSAFE, as illustrated in Fig. 1a, represents a breakthrough in battery-free, skin-adhesive wound electronics. Leveraging the cutting-edge bioelectronic integration strategy, NFC technology and microelectronic fabrication methods, the iSAFE is able to be bioadhered to the wound location and achieve wireless communication and data transfer with the smart terminal (i.e., smartphones) without the need for any battery supplies. The BEWI integrates essential bioactive properties, including biocompatibility, skin adherence, antibacterial action, hemostatic capabilities, gas permeability, and waterproofing, all of which passively enhance wound healing and infection prevention. The iSAFE incorporates stretchable biosensors that in situ monitor glucose, pH, and temperature (Tem) of wound beds, providing critical insights into the wound conditions. At the same time, the smart terminal (i.e., smartphone) can supply power for the iSAFE for intelligent adaptive and on-demand drug release and wound treatment when wound infection occurs (Fig. 1a and Supplementary Fig. 2). As shown in Fig. 1b, c, the iSAFE is designed with an ultra-thin profile and high skin adhesion, featuring a multi-layered stacked layout. The BEWI (~ 60 μm thickness) is constructed by a multifunctional, stretchable, adhesive, antibacterial, co-electrospinning film. Three biosensors play roles in in-situ monitoring the wound conditions, and an on-demand drug release module composed by a pair of voltage-modulated electrodes are responsible for adaptive treatment and drug delivery. Three vertically connected layers of stretchable serpentine traces supported by the stretchable and permeable Tegaderm tape act as connection cables and circuits for wireless communications and power supplies. The overall circuit is small, with a size of 51 mm × 28 mm. Advanced integration strategies have enabled the vertical penetration and connection of three layers of Cu traces with the stretchable biosensors using silver (Ag) paste (Supplementary Fig. 3), resulting in excellent flexibility with an ultrathin thickness of 140 μm (Supplementary Figs. 4 and 5).

Compared to the conventional wound dressings, especially for complex wounds at joint locations, as exhibited in Fig. 1d, the iSAFE is more convenient, comfortable and efficient to apply without bandage and numerous dressings, thereby not hindering the daily activities and life quality of patients. Due to the skin-adhesive and ultrathin features, the iSAFE can be seamlessly adhered to different body locations, especially the joint (like wrist) and bone (like scapula) locations and achieve conformable contact and arbitrary deformation with skin (Fig. 1e and Supplementary Fig. 6) for the in-situ wound monitoring and adaptive treatment by sensor data acquisition, wireless communication and programmed voltage modulation with the NFC technology (Fig. 1f). As every component layer is stretchable, the iSAFE can be bent, twisted and stretched to accommodate realistic body monitoring (Supplementary Fig. 7) and conformally adhered to different wound surfaces (Supplementary Fig. 8). Notably, the Tegaderm (currently widely medical used tape), acted as the substrate and encapsulation layer, exhibits not only gas exchange abilities (Supplementary Fig. 9), but also the wonderful waterproofness. As shown in Supplementary Fig. 10 and Supplementary Videos 1 and 2, the Tegaderm-encapsulated circuit could maintain normal electrical connectivity and not cause a short circuit in phosphate-buffered saline (PBS), even after immersing for seven days. The iSAFE can normally operate, and the LED is still normally lit when the smartphone is closed. As a result, iSAFE can be applied for long-time chronic wound patients and would not affect their daily life and exercise, like running, swimming and even shower. To the best of our knowledge, the iSAFE proposed here for the first time provides a totally battery-free, skin-adhesive, stretchable, permeable, waterproof and multiple-functional intelligent wound electronics with fully bioelectronic integration for in-situ wound monitoring, accelerating wound healing and adaptive treatment (Fig. 1g, Supplementary Fig. 2 and Supplementary Table. 1).

### Design and characterization of Bioactive electronic-wound interface (BEWI)

Figures 2, 3 and Supplementary Note 2 show the characterizations of the BEWI. The fabrication process of the BEWI begins with the co-electrospinning of styrene-ethylene-butylene-styrene (SEBS) containing F127 and gelatin methacrylate (GelMA) that contains anti-bacterial drugs (Fig. 2a). It is well known that SEBS is elastic and biocompatible and GelMA is able to accelerate wound healing[23–25]. So, this strategy strikes a balance among three factors of stretchability, pro-healing,

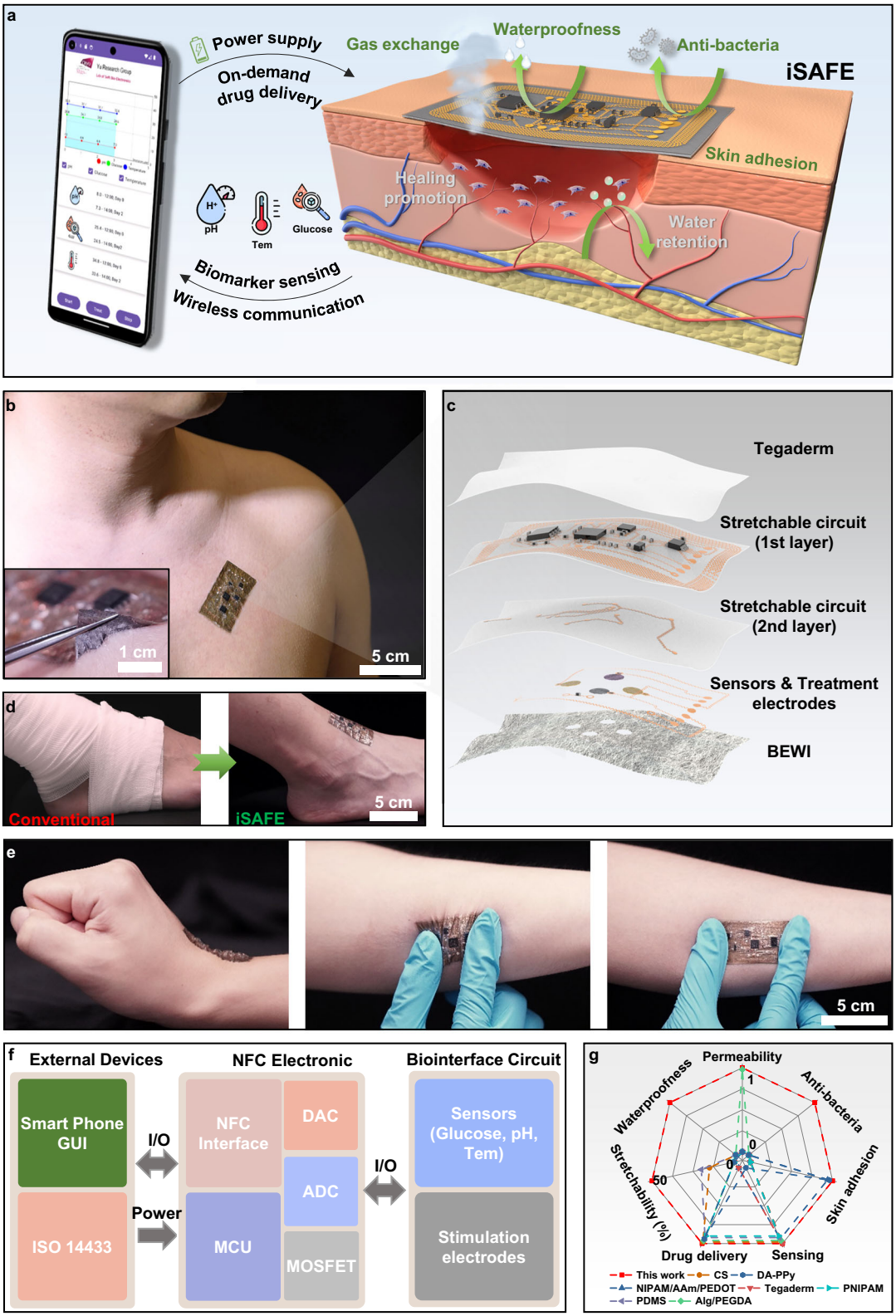


and permeability, and thus provides opportunities for large-scale processing (Supplementary Fig. 11). For further satisfying the requirements of water retention and hydrophilicity for moisture management and exudate absorption around the wound site, we endow the membrane with optimal hydrophilic property by adding Pluronic F127 (an amphiphilic triblock copolymer) into the electrospun SEBS precursor solution, whose hydrophilic block will migrate to the fiber surface of SEBS during electrospinning (Supplementary Fig. 12)[26,27]. After cross-linking the GelMA via UV exposure, the silver nanoparticles (Ag NPs) are in situ synthesized on the fibers by successive immersion in the silver nitrate ($AgNO_3$) and tannic acid (TA) solution. X-ray diffraction (XRD) analysis demonstrates the characteristic diffraction peaks at 38.1, 44.3, and 64.6, corresponding to (111), (200), and (220) crystallographic planes, existed in BEWI

**Fig. 1 | Skin adhesive, battery-free intelligent, stretchable, permeable and multi-functional electronics (iSAFE) system for wound management.** **a** Schematic illustration depicting iSAFE as a multi-functional wound electronic capable of closed-loop sensing and treatment for infected chronic wounds. Highly-integrated configuration endows iSAFE with superior breathability, waterproofness, tissue adhesiveness, anti-bacterial activity, and on-demand therapeutic ability. **b** Optical images of the iSAFE attached onto the chest. The enlarged image demonstrates the robust adhesion of the iSAFE to skin. **c** Exploded-view illustration of iSAFE highlighting key layers. **d** Optical images showing the comparison between conventional wound dressing (left) and our iSAFE (right) for ankle wound treatment. **e** Optical images of the iSAFE system adhering to wrist and arm and its deformation with skin. **f** Block diagram of the key components of the iSAFE system. **g** A radar map comparing the critical performances (i.e., permeability, anti-bacterial ability, skin adhesion, stretchability, waterproofness, sensing, and drug delivery) of our iSAFE against other published systems.

(Fig. 2b). These findings are in line with SEM images, EDS, FTIR and XPS results (Supplementary Figs. 13 and 14), indicating successful synthesis of AgNPs mediated by TA. In addition, molecular dynamics simulation reveals multiple interaction effects, including hydrogen bonding and electrostatic attraction are involved in the anchoring of AgNPs onto the surface of electrospun membrane (Supplementary Fig. 15). To optimize the performance of the BEWI, we explored the impact of SEBS and GelMA fiber ratio on the conductivity. As shown in Fig. 2c, all the BEWIs with different ratios of SEBS to GelMA show good conductivity of around 0.52 S/m, demonstrating the conductivity is predominantly dependent on the loading amount of Ag NPs, rather than the SEBS/GelMA (S/G) ratio.

Figure 2d and Supplementary Fig. 16 show the stress-strain curves of GelMA, S/G fibers with different content ratios. It is clear that the co-electrospinning strategy largely improves the stretchability of the fibers and the stretchability is enhanced with the increase of SEBS content. In addition, the mechanical strength and stretchability of BEWI (SEBS: GelMA 1:1) are further increased because of the enhanced intermolecular interactions by TA (Supplementary Fig. 17). TA is a polyphenolic compound rich in hydroxyl groups that can form strong hydrogen bonds with the amine and hydroxyl groups present in the GelMA polymer chains. This additional crosslinking via hydrogen bonding results in a denser network structure, leading to improved mechanical properties like higher tensile strength and stretchability[28,29]. As a result, the BEWI with a SEBS: GelMA ratio of 1:1 would be the optimal choice by balancing the mechanical and biological performance. Besides, the resistance responses of the optimized BEWI under the stretching configure are tested. As shown in Supplementary Fig. 18, the resistance change is negligible under 10 % and 30 % stretching. Although there are changes of the resistance of the BEWI when stretched to 50 %, the resistance could return to the initial state, and the tiny fluctuation is not enough to influence the electrical performance of BEWI. In addition, the resistance exhibited stable recovery capabilities even after undergoing in excess of 600 cycles of continuous 50 % stretching/releasing, suggesting its ability to meet the electrical requirements of a bioelectrical interface applied on a dynamic wound surface. Furthermore, BEWI shows appropriate biodegradability (~ 40 % mass loss during 14-day testing in collagenase solution), water vapor transmission rate (WVTR) (~ 50 g/m$^2$/h), and swellability (~ 300%) (Fig. 2e–g). And the iSAFE with encapsulation shows good water retention ability and can maintain the moisture environment around wound locations (Supplementary Fig. 19). Due to multiple synergistic interactions, including hydrogen bond and Schiff-base/Michael addition reaction, electrostatic attraction, cation-π interaction (Fig. 2l), BEWI exhibits good tissue adhesiveness, which can conformally attach to the skin surface even under twisting and bending (Supplementary Figs. 20–22). Quantitative analysis shows the shear strength and peel-off strength of BEWI are much higher than those of commercial fibrin glue, demonstrating its clinical application potential (Fig. 2h–k). Besides, the BEWI shows superior wet-resistant skin adhesion on pork skin (Supplementary Fig. 23). And the interface can be removed once the wound has fully healed. The adhesive interface can be treated with a urea solution to render it non-adhesive (Supplementary Fig. 24); this process involves disrupting the existing hydrogen bonds to reduce the bond strength at the interface[30,31]. Furthermore, the removed device can be subjected to additional processing and recycling, which includes the removal of the adhesive electrospun interface layer while retaining the upper electronic layer. And the alternative interface provides conveniences for avoiding severe foreign body responses and chronic fibrotic encapsulation[32–34].

Next, we evaluate the in vitro bioactivity of BEWI. First, live/dead staining and cell counting kit-8 (CCK-8) assay indicate the favorable biocompatibility of BEWI, which can facilitate cell survival and proliferation (Fig. 3a–c), which may be due to the strong bonding to TA within the matrix impeding the release of Ag NPs[35]. Wound healing assay, also known as the cell scratch test, further demonstrates BEWI can promote cell migration and accelerate wound healing rate (~ 90% wound closure within 48 h) (Fig. 3d, e and Supplementary Fig. 25). In addition, we find that such composite membrane supports cell adhesion (Supplementary Fig. 26) and possesses excellent anti-bacterial activity (Fig. 3f, g, and Supplementary Fig. 27), suggesting it can create a beneficial microenvironment for cell growth and shows promising potential as an anti-infective wound interfacial material. For some serious pathogens that hard to kill (like Pseudomonas aeruginosa (*P. aeruginosa*)), the anti-bacterial performance can be achieved by changing the targeted drug in the BEWI (Supplementary Fig. 28). We further evaluate the hemostasis of the BEWI by the tail and liver hemostatic models. As shown in Supplementary Figs. 29 and 30, compared to the control group (without the BEWI), the blood losses in the BEWI groups are much lower no matter for the tail or liver hemostatic models, revealing the great hemostasis of the BEWI.

## Stretchable multiple biosensors for in-situ wound monitoring

In order to enhance the stretchability of the biosensors, we design stretchable electrodes based on advanced fabrication strategies (Supplementary Note 3). Benefitting from the pre-stretching strategy, the conductive SEBS can ensure basically stable resistance even under the stretching state (Fig. 4a). As exhibited in Supplementary Figs. 31–33, the pre-stretched SEBS enables to retain stable resistance even under continuous stretching and friction compared to the normal sputtering SEBS fiber. Based on the stretchable gold (Au) coated SEBS electrodes, glucose and pH biosensors are constructed by modifying the corresponding sensing elements (Supplementary Fig. 34). Several holes are laser-cut into the BEWI for the direct contact of sensors with wound exudate without negative impact on the functions of BEWI (Fig. 4b). Figure 4c–e show the responses of glucose, pH and Tem sensors as a function of time, and Fig. 4f–h demonstrate their corresponding calibration curves. As shown in Fig. 4c, f, the current response of the glucose sensor increases with the increased glucose concentration in the electrolyte, and there is great linearity between the glucose concentration in the electrolyte and the current output of the glucose sensor. Similarly, the voltage outputs of the pH sensor could decrease with the increased pH values, and the outputs are linearly related to the pH values. For the Tem sensor composed of the negative Tem coefficient (NTC) thermistor, the resistance of the thermistor decreases with increasing Tem in an excellent linearity. Supplementary Figs. 35 and 36 show the superior stretchability, stability, repeatability and reliability of the glucose and pH sensors. The electrical outputs of the two sensors could even maintain a relatively stable value under 30 % continuous stretching. Anti-interference tests shown in Supplementary Figs. 36a and **b** indicate that the outputs of glucose and pH sensors would not be affected by other metabolites.

https://doi.org/10.1038/s41467-025-61261-8

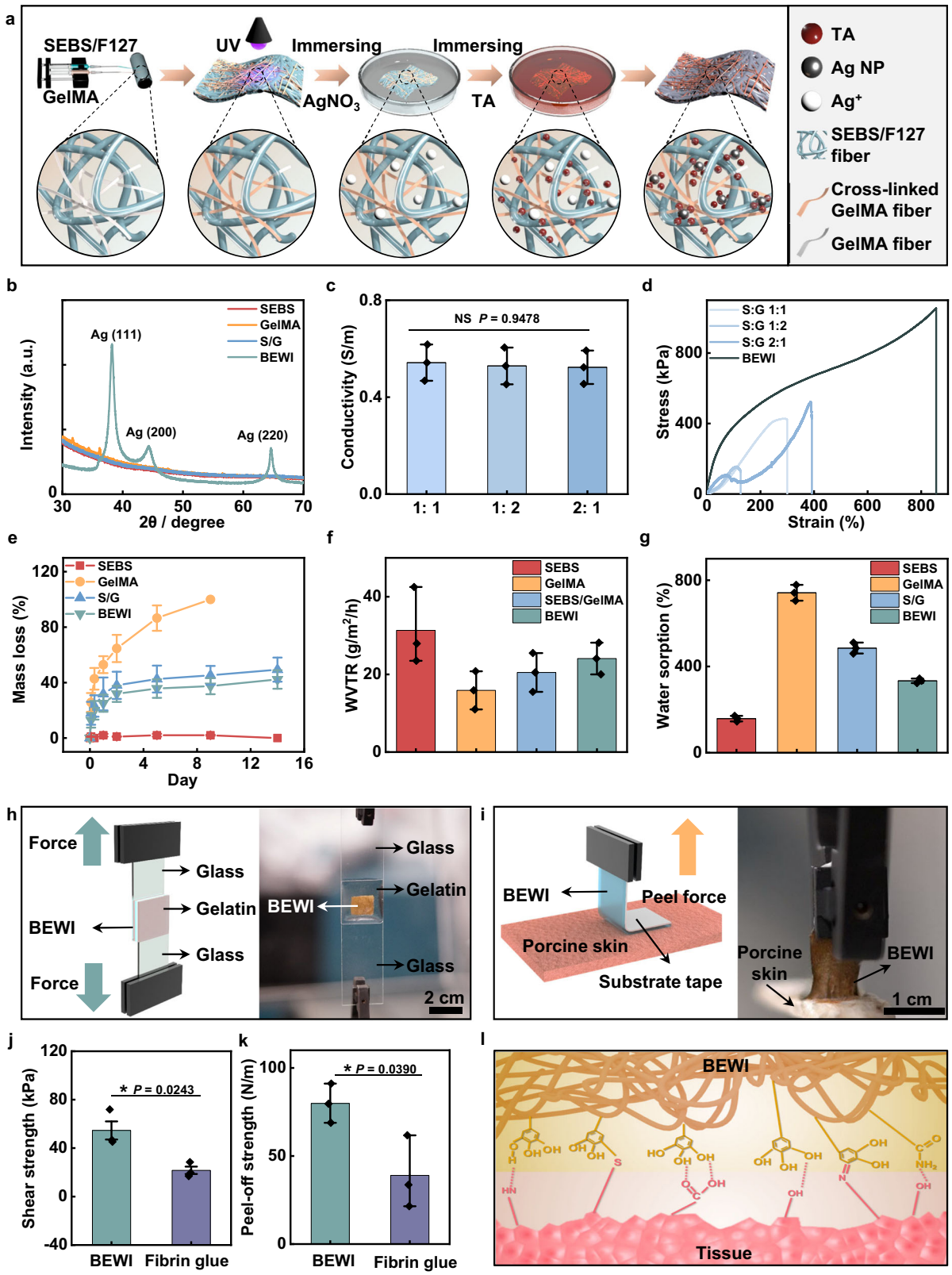


Repeated tests for the same glucose and pH sensors show stable output signals for a continuous monitoring of 5 days (Supplementary Figs. 36c, d). These results benefit the superior stability and specificity of the sensing elements of glucose oxidase (GOx) and iridium oxide ($IrO_x$). And the superior effectiveness and generalizability of these sensing principles have been widely proved[36–40]. Similarly, as shown in the Supplementary Figs. 36e, f, the Tem sensor has great stability, repeatability and reliability. As for other wound exudate matrices, such as protein, cells, etc., we select bovine serum albumin (BSA, 10 mg/mL) as a demonstration here to test the stability of the glucose and pH sensors. BSA is a kind of widely used large macromolecule serving as a standard protein in various biochemical assays. As shown in Supplementary Fig. 37, although some fluctuations observed after dropping BSA on the sensor surface, the outputs would go back to the initial

**Fig. 2 | Preparation and characterization of the bioadhesive, multifunctional BEWI. a** Schematic illustration of the fabrication process of the BEWI. **b** XRD patterns of the electrospun SEBS, GelMA, SEBS/GelMA and BEWI films. **c** Conductivities of BEWIs with different ratios of SEBS and GelMA (w/w) ($n = 3$ independent replicates, one-way two-sided analysis of variance test, NS denotes not significant, mean value ± SD). **d** Stress-strain curves of different electrospun films. **e** Mass loss of the electrospun SEBS, GelMA, SEBS/GelMA and BEWI films after incubation in PBS containing collagenase (3 μ/mL) for 14 days ($n = 3$ independent replicates, mean value ± SD). **f** Water vapor transmission rate and (**g**) water sorption of different electrospun films ($n = 3$ independent replicates, mean value ± SD). Schematics and optical images and of the (**h**) lap shear and (**i**) peel-off tests. Comparison of (**j**) shear strength and (**k**) peel-off strength between BEWI and commercial fibrin glue ($n = 3$ independent replicates, Two-sided Student's $t$ test, $^*P < 0.05$, mean value ± SD). **l** Schematic illustration showing the mechanism of tissue adhesiveness of BEWI. SEBS mentioned in this work represents the hydrophilic SEBS/F127.

value eventually. The fluctuations may be caused by the physical interaction and spreading of the BSA droplet on the sensor surface during pipette addition. As these sensors are intended for monitoring wound exudate and will be in direct contact with open tissue, biocompatibility is a paramount consideration that must be given primacy. The cell co-culture results, as exhibited in Fig. 4i–k, indicate that there is no obvious cytotoxicity of the sensing elements, electrodes and other components of glucose, pH and Tem sensors. As a result, the integrated sensors of glucose, pH and temperature in the iSAFE all exhibit superior performance in the perspective of stretchability, stability, and sensitivity and can totally satisfy the requirements of skin-integrated wound monitoring (Supplementary Tables. 2–4).

## Battery-free wireless communication and on-demand drug release

For achieving battery-free wireless communication and control, NFC is applied for wireless power supply and data transmission to the smartphone. Supplementary Figs. 38 and 39 outline the circuit and block diagrams of the control circuit. A system-on-a-chip microcontroller (MCU) is employed for data processing, acquisition and storage from the patch. An N-type MOSFET is used as a switch to control the drug delivery. The analog signal outputs collected from the sensors can be converted into digital signals by a 12-bit analog-to-digital converter (ADC) and then transmitted to the MCU. Finally, the collected data with a sampling frequency of 10 Hz is transferred to the smartphone via the NFC antenna without requiring user intervention when the smartphone is brought in proximity. Supplementary Fig. 40 shows the stability and stretchability of the circuit with a wide and stable wireless communication and voltage output. Supplementary Fig. 41 shows the controlled drug delivery by iontophoresis and programmed voltage. When an infection occurs and is detected by sensors, the anti-infection drug contained in BEWI (like antibiotics) can be released to the wound bed (Supplementary Fig. 41a). As shown in Supplementary Figs. 41b, c, the drug release amount is well controlled by both the applied voltage value and duration time, while the amount can be negligible when no voltage is applied to BEWI. Besides, the drug contained in BEWI is an alternative, we can apply the targeted drug for some complex and severe infections led by the pathogens that hard to kill. It could be seen in the Supplementary Fig. 41d that the drug release strategy is also suitable for other charged drugs. The release rates of various drugs are largely different because of the differences in drug molecular sizes, and drug ionization and drug charge states[41]. The controlled localized drug delivery is an additional therapy strategy when infection happens, which would not only enhance the efficacy of the treatment by ensuring a sustained and optimal concentration of the therapeutic agent at the site of action but also minimize systemic side effects and drug abuse. Furthermore, Supplementary Fig. 42 shows the drug delivery efficiency comparison after soaking in water for 3 days. The stable drug release amount without excessive leakage in water can be attributed to the formation of TA-Ag complexes on electrospun fibers, which could act as a physical barrier to increase the drug diffusion route into the surrounding solution[35].

## In vivo preclinical study of the iSAFE system

Figures 5, 6 and Supplementary Note 4 show the in vivo evaluation on diabetic rats to test the robustness and efficacy of the iSAFE in wound monitoring and accelerating wound healing. As exhibited in Fig. 5a and Supplementary Video 3, the iSAFE can be seamlessly attached to the back of the rat and our developed state-of-the-art biosensors are able to monitor wound state by the graphical user interface (GUI) (Fig. 5a). For the diabetic rats, bilateral full-thickness excisional wounds infected with *E. coli* (20 μl, $10^6$ CFU/mL) are established at first (at day -1) (Supplementary Fig. 43). Here, three different groups are tested for verifying the validity of the iSAFE: Control group (Tegaderm dressing without controlled drug release), S/G/P group (prinstine electrospun S/G/Drug film) and iSAFE group. From day 0 to day 6, we measure the glucose level, pH and Tem of the wound exudate and exchange wound dressings every two days for each group. The mixed bacteria colonies culture from the wound beds of three different groups onto LB agar plates shows a significant decrease in bacteria growth in the iSAFE group as compared to the other two groups, proving the excellent antibacterial properties of the BEWI and iSAFE (Supplementary Fig. 44). As shown in Fig. 5b and Supplementary Fig. 45, the highest wound closure rate is observed in the iSAFE group, while that of the S/G/P group is higher than the control group, demonstrating the effectiveness of the iSAFE on the pro-healing. The pro-healing performance of the S/G/P group may be led by the presence of GelMA with the drug. As shown in Fig. 5c, the glucose levels in wound exudate would decrease for infected wounds. The recovery of glucose concentration in the wound presents the infection cleaning and wound healing[17,42]. While it could be seen that the overall tendency of the three groups of pH and Tem value decreases, meaning that the appearance of wound healing (Fig. 5d, e)[18,43]. The obvious comparison results in the iSAFE group compared to other groups demonstrate the excellent ability of iSAFE to combat bacteria and promote chronic wound healing.

To evaluate the healing effectiveness of the three group wound dressings, we further perform hematoxylin and eosin (H&E), Masson's trichrome (MT) staining and immunochemistry and immunofluorescence analyses of the wound tissues after 6 days and 14 days, respectively. On the 6th day, as exhibited in Supplementary Fig. 46, although tissue defects and inflammatory cell infiltration could be observed in each group, the wound healing stages are largely different for the three groups. On the 14th day, the wound is almost healed in the iSAFE group while partial tissue defects could be seen in other two groups (Fig. 5f). For the quantity analysis of H&E staining, it is obvious that the wound indexes of epidermal thickness of the iSAFE group are largely higher than those of the control and S/G/P groups while the length of wound area of the iSAFE group is less than the other two groups on the 6th day (Fig. 5g). On the 14th day, mature epithelium, higher epidermal thickness, re-epithelialization, and dermal appendage count as well as lower length of wound area and scar elevation index are observed in H&E staining results of the iSAFE group (Fig. 5f, g–i). The MT staining images and quantity analysis results (Fig. 5f, j–l) exhibit a significantly higher collagen density for the iSAFE group compared to the other two groups, demonstrating the granulation tissue formation and uniform dermis repair.

In order to further explore the inflammatory response and mechanism of the anti-inflammatory and accelerating wound dressing of the iSAFE system, we then perform the immunochemical staining and transcriptomic sequencing analysis of the wound tissue after 6-day treatment, which indicates the transition from the inflammatory phase to the proliferation phase during normal wound healing.

https://doi.org/10.1038/s41467-025-61261-8

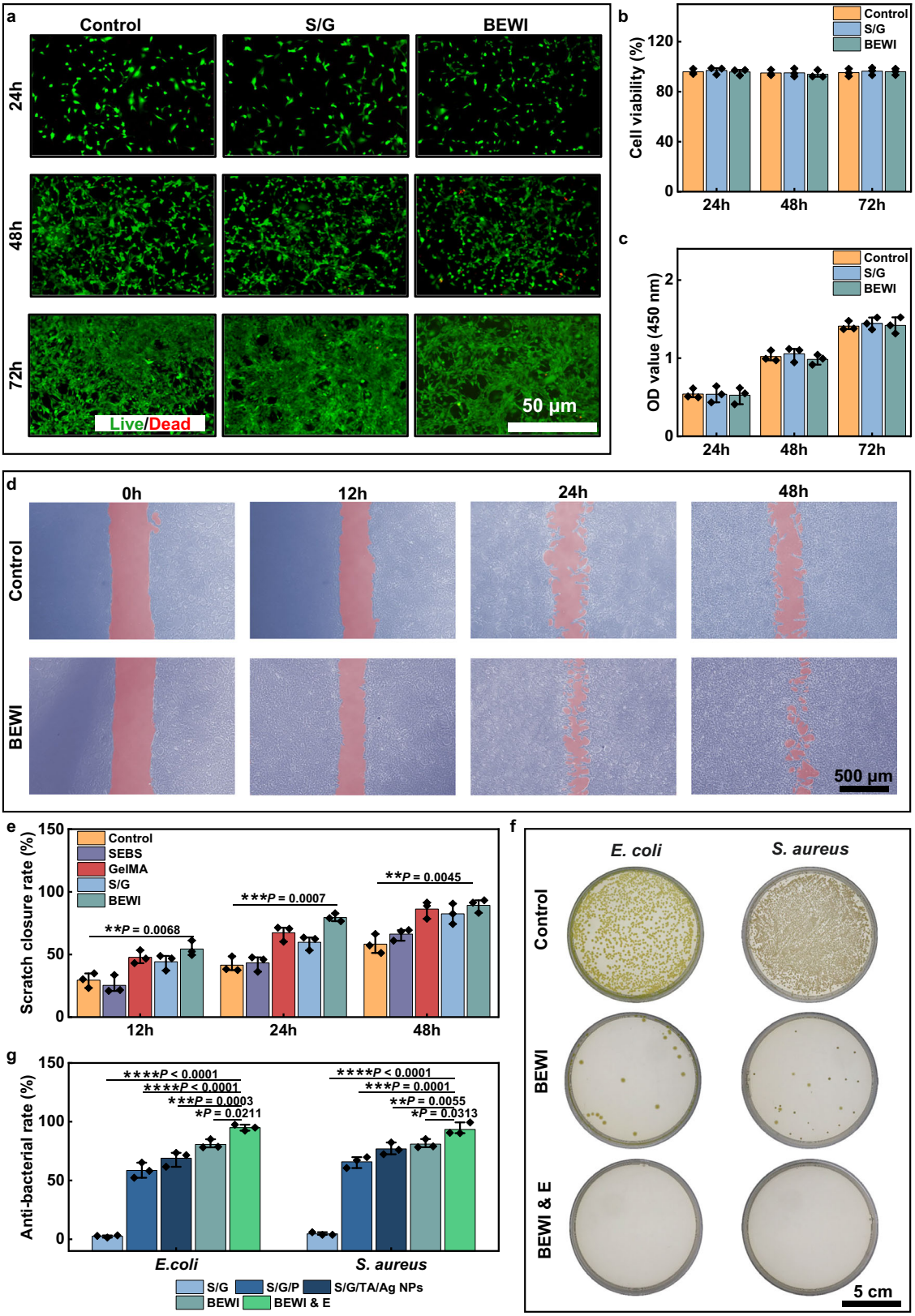


**Fig. 3 | In vitro evaluation of biocompatibility, pro-healing, and anti-bacterial performances of BEWI. a** Live/dead staining of NIH/3T3 cells cultured with different materials for 24, 48, and 72 h. **b** Cell viability calculated based on live/dead staining images ($n = 3$ independent replicates, mean value ± SD). **c** Cell proliferation evaluation via CCK-8 test ($n = 3$ independent replicates, mean value ± SD). **d** Scratch assay to analyze the migration ability of NIH/3T3 cells pretreated with BEWI. Control is the group without BEWI treatment. **e** Quantification of the scratch closure rate ($n = 3$ independent replicates, one-way two-sided analysis of variance test, $^{**}P < 0.01$, $^{***}P < 0.001$, mean value ± SD). **f** Images of cultivated *E. coli* and *S. aureus* colonies onto Luria-Bertani (LB) agar plates after being treated with different materials. **g** Quantitative assessment of anti-bacterial rate of various materials against *E. coli* and *S. aureus* ($n = 3$ independent replicates, one-way two-sided analysis of variance test, mean value ± SD). For the *E. coli* group, $^{****}P < 0.0001$, $^{***}P = 0.0003$ and, $^{*}P = 0.0211$. For the *S. aureus* group, $^{****}P < 0.0001$, $^{***}P = 0.0001$, $^{**}P = 0.0055$ and, $^{*}P = 0.0313$.

https://doi.org/10.1038/s41467-025-61261-8

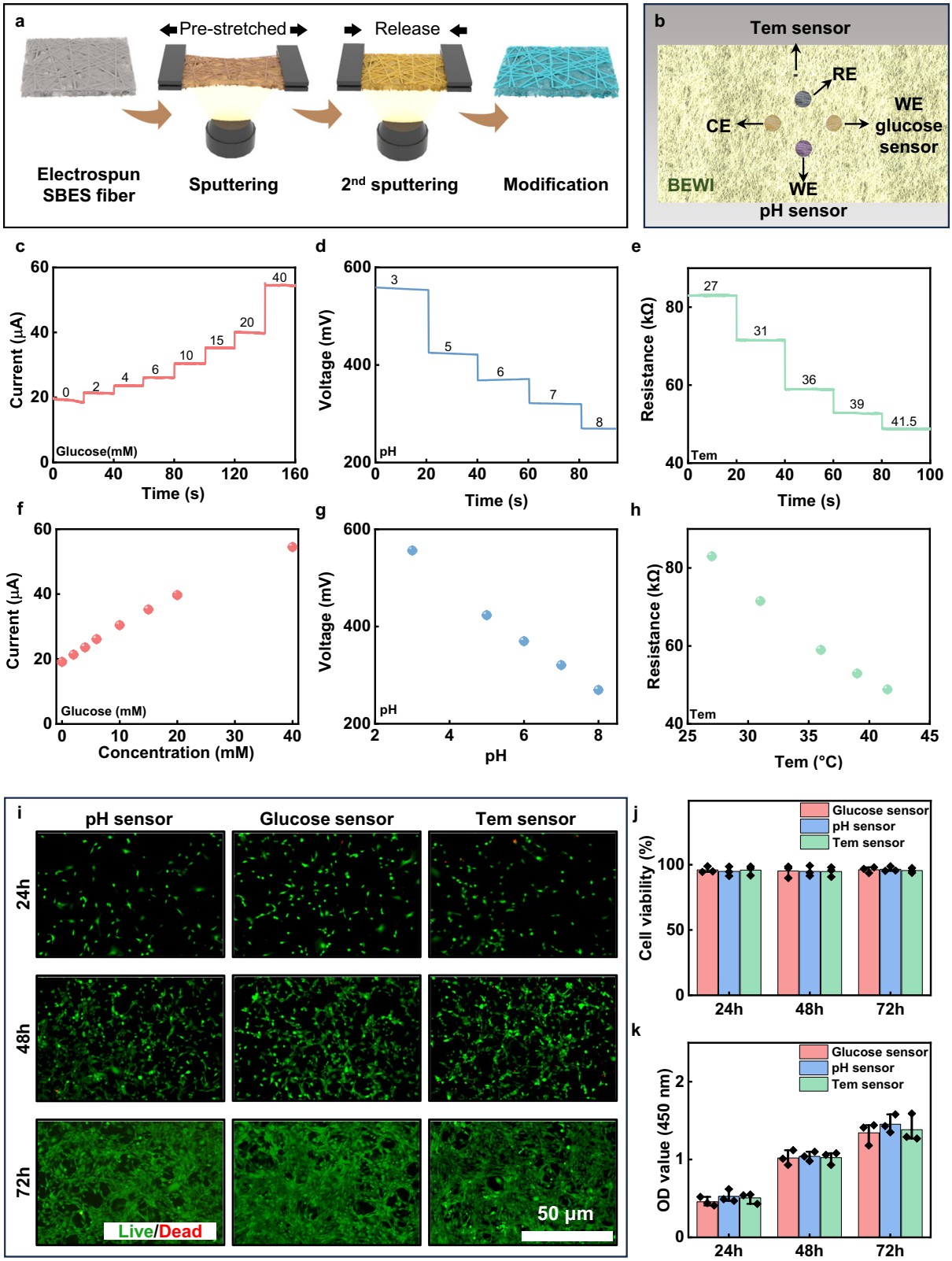


**Fig. 4 | Characterization of stretchable biosensors based on the electrospun SEBS film. a** Schematic illustration of the fabrication process of the stretchable SEBS electrode. **b** Schematic illustration showing the electrode layout of working electrode (i.e., thermal, pH and glucose sensors), counter electrode (CE) and reference electrode (RE) onto BEWI. **c**–**e** Output responses of the glucose, pH and Tem sensors as a function of time. **f**–**h** Corresponding calibration curves of the glucose, pH and Tem sensors. **i** Biocompatibility evaluation of pH, glucose and Tem sensors by live/dead staining. Quantitative analysis of (**j**) cell viability and (**k**) cell proliferation co-cultured with different specimens ($n = 3$ independent replicates, mean value ± SD).

https://doi.org/10.1038/s41467-025-61261-8

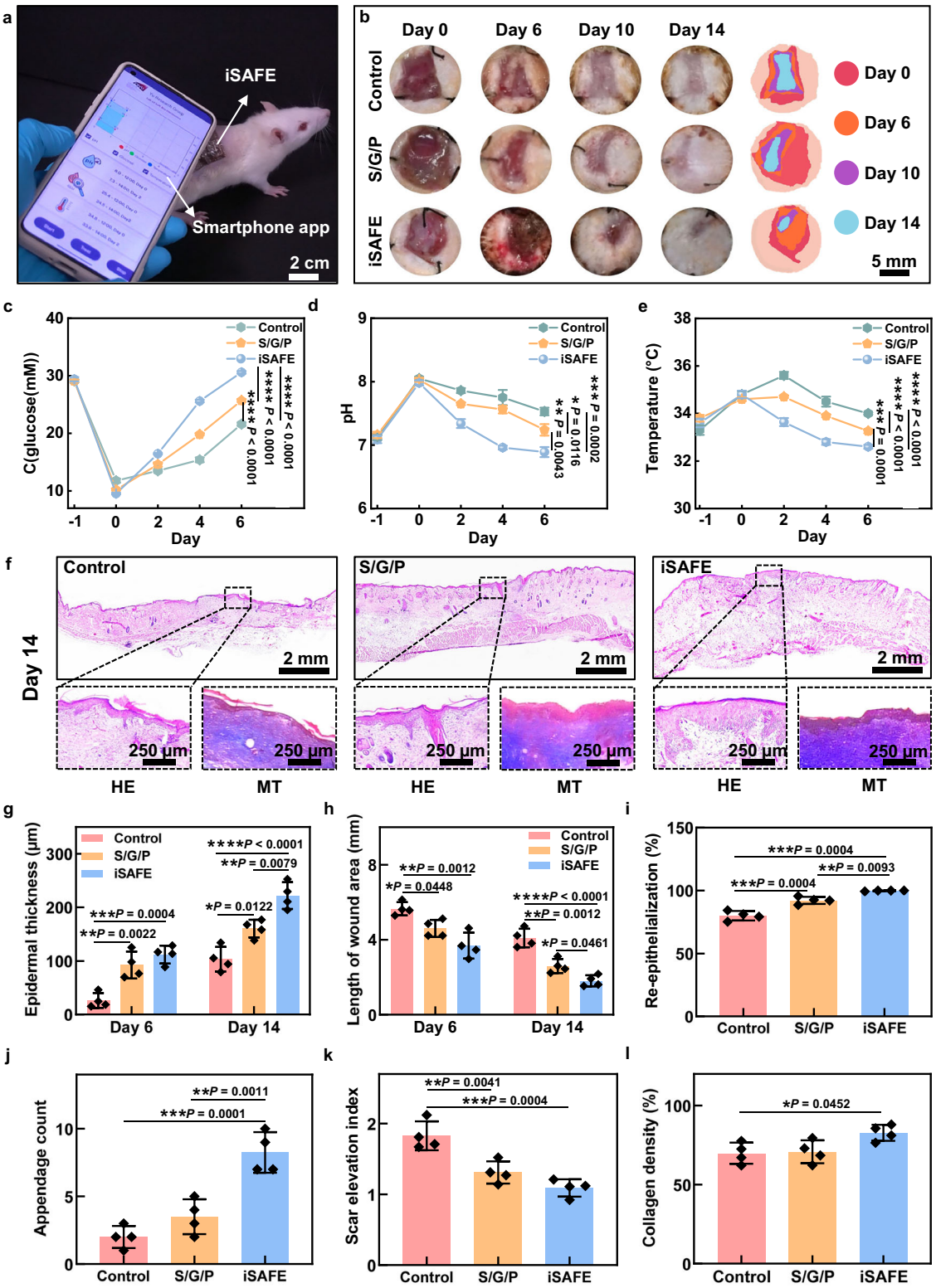


**Fig. 5 | In vivo investigation of iSAFE for in-situ wound monitoring and accelerated wound healing. a** Optical image of iSAFE adhered to the rat with a chronic wound on its back for in-situ wound monitoring and therapy. **b** Representative images and schematic illustrations showing the change of diabetic infected wounds with time after different treatments. In-situ measurement of dynamic changes of (**c**) glucose concentration, (**d**) pH and (**e**) Tem in the infected diabetic wound with different treatments ($n = 3$ independent replicates, one-way two-sided analysis of variance test, $^{*}P < 0.05$, $^{**}P < 0.01$, $^{***}P < 0.001$ and $^{****}P < 0.0001$, mean value ± SD). **f** Representative histologic images of wound tissues harvested from diabetic rats with different treatments for 14 days. Top and bottom left, hematoxylin and eosin (H&E); bottom right, Masson's trichrome (MT). Quantitative analysis of (**g**) epidermal thickness, (**h**) length of wound area, (**i**) re-epithelialization, (**j**) appendage count, (**k**) scar elevation index and (**l**) collagen density of skin tissues after different treatments ($n = 3$ independent replicates, one-way two-sided analysis of variance test, $^{*}P < 0.05$, $^{**}P < 0.01$, $^{***}P < 0.001$ and $^{****}P < 0.0001$, mean value ± SD).

https://doi.org/10.1038/s41467-025-61261-8

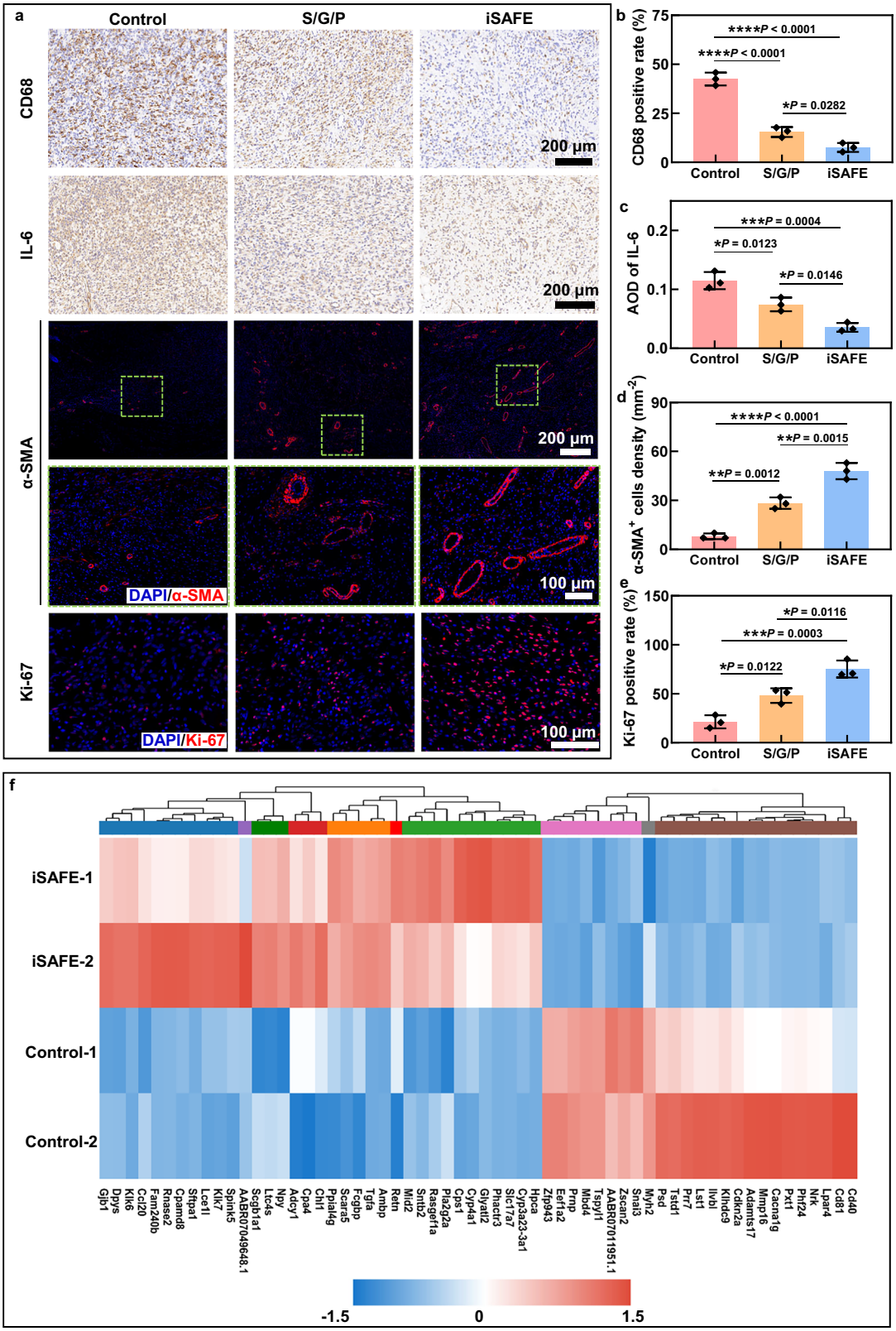


**Fig. 6 | Mechanism analysis of the wound healed through iSAFE treatment.** Representative immunostaining images for (**a**) cluster of differentiation 68 (CD68), interleukin 6 (IL-6), alpha smooth muscle actin (α-SMA) and Ki-67 (red) (Cell nuclei were stained with 4′, 6-diamidino-2-phenylindole (DAPI, blue)) from wound tissues after different treatments. Quantity analysis of the IHC staining (**b**) CD 68 positive rate, (**c**) average optical density (AOD) of IL-6, (**d**) α-SMA$^+$ cells density, and (**e**) Ki-67 positive density of wounds with three different wound dressings after 6 days treatment ($n = 3$ independent replicates, one-way two-sided analysis of variance test, $^*P < 0.05$, $^{**}P < 0.01$, $^{***}P < 0.001$ and $^{****}P < 0.0001$, mean value ± SD). **f** Heatmap showing the comparison of differentially expressed genes (DEGs) in the wound tissues between the control group and the iSAFE treatment group ($P < 0.05$).

Immunochemical staining of innate immune macrophage marker (i.e., CD68) and pro-inflammatory marker (i.e., IL-6) at day 6 demonstrates the significantly reduced inflammatory response in iSAFE (Fig. 6a–c). In addition, the expression level of α-SMA, a marker of vascular smooth muscle cells commonly used to assess blood vessel formation within wound, is also much higher in iSAFE (Fig. 6a, d). Meanwhile, the immunofluorescent staining of Ki-67, a classic marker for normally proliferating cells, demonstrates obviously the higher expression level of Ki-67 in the iSAFE group at day 14 (Fig. 6a, e). Most importantly, all of these materials display no obvious impairment to major organs like heart, kidney, liver and spleen, showing good in vivo biocompatibility (Supplementary Fig. 47). These results collectively indicate that iSAFE is biocompatible and can alleviate inflammation at early stages of wound healing, while promoting cell proliferation and angiogenesis at subsequent stages. These attributes are directly associated with the wound healing cascade and are thus considered favorable for expediting skin repair.

For the transcriptomic sequencing analysis, as shown in Supplementary Fig. 48, there are totally 497 differentially expressed genes (DEGs) discovered in the iSAFE group compared to the control group, including 285 up-regulated genes and 212 down-regulated genes. The heat map of DEGs, as shown in Fig. 6f exhibits significant differences of the transcriptome profile between the iSAFE group and control group, including genes closely related to the immune response (like CD40 and CD81)[44–46] and skin repair (like Klk6)[47]. To clarify the functions of the identified DEGs, Gene Ontology (GO) annotation and Kyoto Encyclopedia of Genes and Genomes (KEGG) pathway analysis are developed. As exhibited in Supplementary Figs. 49 and 50, GO annotations and enrichment analysis (top 15 of abundance) reveal muscle tissue development and cell growth, etc., and downregulation of immune response, etc. KEGG pathway analysis of DEGs (top 15 of abundance) finds that the application of iSAFE has a significant regulatory impact on pathways oxidative phosphorylation, thermogenesis and NF-κB signaling pathways, etc (Supplementary Figs. 51 and 52)[48–50]. These results additionally prove the anti-inflammatory and pro-healing effects of iSAFE from the perspective of molecular and gene regulation.

### Clinical study of multiple biosensors

Clinical application serves the pivotal goal for wearable medical device development, guiding the translation of technological advancements into tangible benefits for personalized medicine. We endeavored, to the greatest extent possible, to employ the iSAFE in clinical trials for detecting wound exudate (Fig. 7 and Supplementary Note 4). This aims to determine wound healing or infection conditions, thereby providing directions for targeted treatment interventions. As shown in Figs. 7a–c and Supplementary Fig. 53, we apply the iSAFEs for a diverse cohort of 10 patients with different ages, genders, body mass indexes (BMIs), and wound types. Therein, we longitudinally monitored the pH, glucose and Tem in wound exudate during two-weeks treatments for six patients (No.1 to No. 6) and detected wound exudate one time for four patients in the ward (No.7 to No. 10). At the same time, we recorded their wound size, depth/undermining (UM) and morphology (Supplementary Figs. 54 to **60** and Supplementary Table. 5). During detection periods, we compared with the results assessed by our developed biosensors with those of commercial instruments. As shown in Fig. 7d–f and Supplementary Fig. 61, the sensors of glucose, pH and Tem all show good accuracy more than 80%, with low errors. Based on the detection results, the triangle of wound assessment (Supplementary Fig. 62)[51] and wound bed score (WBS) (Supplementary Table. 6)[52], we additionally employed the patient-specific correlation using Pearson's correlation coefficients between the glucose, pH and Tem of wound exudate and WBS. As demonstrated in Fig. 7g, statistically significant negative correlations between pH and WBS, as well as Tem and WBS, can be observed in all 6 patients, proving the feasibility of selecting these parameters for wound assessment and providing treatment directions. For the correlation between the glucose concentration in wound exudate and WBS, it could be seen that there is a positive correlation for most patients. Reduced healing rates in diabetic patients (No. 2 and No. 3) are observed compared to normoglycemic patients. This emphasizes the relevance of regular glucose monitoring in wound exudate for effective wound management. Variations in correlation between glucose and WBS could be attributed to factors like meal and measurement times, and medication regimens. Ultimately, the overall partial correlation analysis results reveal significant negative correlations among the pH, Tem of exudate and WBS and a positive correlation between glucose concentration in wound exudate and WBS (Supplementary Fig. 63).

## Discussion

In summary, we have developed a fully stretchable, skin-adhesive, permeable, waterproof and multifunctional wound electronics capable of in-situ monitoring wound exudate, accelerating wound healing and enabling intelligent wound treatment. The iSAFE system comprises a bioactive electronic-wound interface (BEWI), a stretchable multimodal biosensor array, an adaptive drug release module, as well as encapsulated, stretchable and permeable control circuits. The iSAFE system is biocompatible, skin-conformal and ultrathin, with a similar thickness of the epidermis, allowing it to adhere to various body locations. The encapsulated circuit layer is permeable and waterproof, facilitating gas exchange while preventing bacteria and short circuits. The BEWI exhibits superior skin-adhesion, antibacterial properties and pro-healing performance, coupled with excellent stretchability and permeability. The state-of-the-art biosensor array of glucose, pH and Tem based on the stretchable electrodes displays remarkable sensitivity, linearity, stretchability and stability. Consequently, the iSAFE system can not only prevent wound infection and accelerate wound healing but also achieve closed-loop feedback between in-situ wound monitoring and intelligent treatment. Both in vitro and in vivo study results demonstrate the effectiveness of iSAFE in comprehensive wound care. Furthermore, clinical evaluations indicate the practicability of sensing functions of iSAFE and its ability to show wound healing stages and direct treatment interventions. Altogether, the integrated solution of iSAFE for real-time wound assessment, bioactive interface, and intelligent medication administration has not only demonstrated superior diagnostic and therapeutic capabilities but has also successfully streamlined these functions into an efficient, non-disruptive synergy, engendering a new paradigm in wound electronics and offering promising benefits for the seamless combination of biological materials and electronics for both epidermal and implantable applications.

In the future, research involving a randomized controlled trial with expanded patient cases will provide additional validation for our preliminary results about the prognostic significance of these biomarkers in predicting the status of wound healing and directing wound treatment. Future investigation would also focus on developing a state-of-the-art microfluidic wound fluid sampling system with skin-adhesion and permeability for efficient capture and continuous delivery of wound fluid to the sensor chamber to improve the temporal resolution of in situ biomarker detection[14,20]. Besides, chronic fibrotic encapsulation remains a persistent challenge, necessitating disruptive surgical retrieval. This issue is a key limitation in the field and requires further investigation. Future research would pay more attention to addressing long-time implantation and foreign body response with mechanical interlocking or penetration between biomaterials and tissue.

## Methods

### Fabrication of the BEWI

For fabricating a fibrous mat composed of SEBS and GelMA, a co-electrospinning setup was employed. This setup consisted of two parallel 20-mL syringes connected to a dual-channel syringe pump.

https://doi.org/10.1038/s41467-025-61261-8

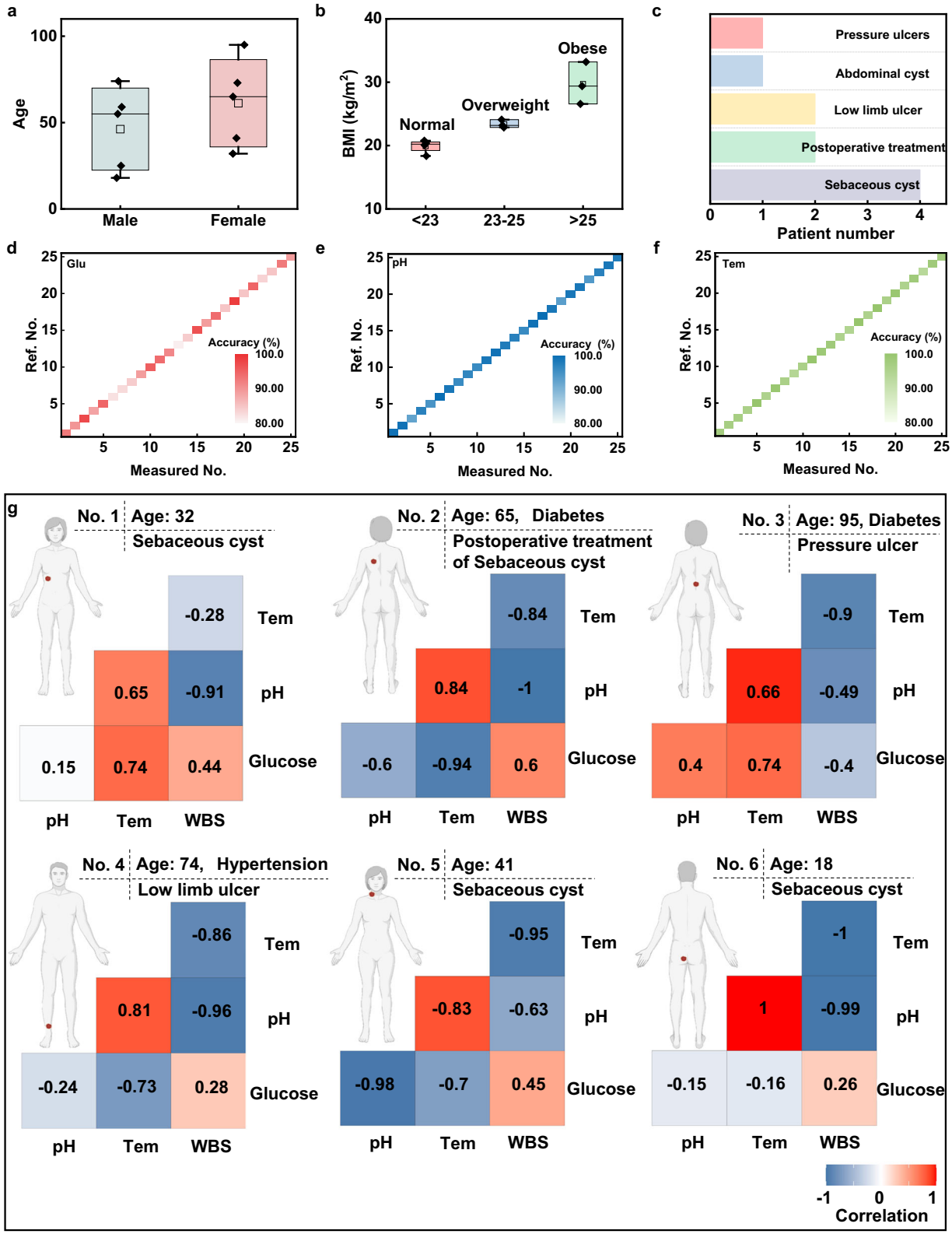


**Fig. 7 | Clinical assessment of the in situ wound monitoring glucose, pH and Tem. a** Box plot showing the age and gender distribution of 10 enrolled patients. **b** Box plot showing the BMI distribution. Here, the normal number is 4 ($n = 4$), the overweight number is 3 ($n = 3$), and the obese number is 3 ($n = 3$). Minima, maxima, center, bounds of the box and whiskers and percentiles are shown in the box plots of (**a** and **b**). **c** Column plot displaying the diseases distribution in these 10 patients. Analysis of the accuracy rate of (**d**) glucose, (**e**) pH and (**f**) Tem sensors in the iSAFE system by comparing with data collected from commercial instruments. **g** Patient-specific correlation matrices of parameters assessed by sensors and the wound bed score (WBS) for the 6 tracked patients. The scale bar represents Pearson's correlation coefficient ($r_p$). Part elements in this figure were *Created in BioRender. H, K. (2025)* https://BioRender.com/nd4kln3.

One syringe contained a mixing solution of SEBS with a flow rate of 0.8 ml/h, while the other syringe contains a mixed GelMA/antibiotics solution (10 wt.% GelMA and 0.2 wt.% penicillin sodium in hexafluoroisopropanol) with a flow rate of 1.0 ml/h. The SEBS solution was obtained by solving SEBS (80 wt.%) and F127 (20 wt.%) in chloroform (80 wt.%) and toluene (20 wt.%). Both syringes were equipped with 21 G metal nozzles. To ensure a uniform distribution of the fibrous mat, the x-axial sliding speed of the needles was set between 10–12 mm/s. A voltage ranging from 18 to 23 kV was applied to the solutions, with the positive electrode attached to the nozzles. The fibers were collected on aluminum foil covering a 10 cm diameter drum, which rotated at 90–100 revolutions per minute and was positioned 15 cm from the nozzle tips. The entire process was conducted over 12 h. All reagents used here are ACS reagents (≥99.0%).

After obtaining the co-electrospun film, the GelMA fiber in the film was cross-linked in the solution of 2-Hydroxy-4′-(2-hydroxyethoxy)-2-methylpropiophenone (photoinitiator 2959, 8 wt.%) with UV exposure for 8 min prior to peeling off from the substrate. Following, the film was immersed in the Ag $NO_3$ (1.5 wt.%) and TA (10 wt.%) solution sequently to achieve the BEWI.

### Fabrication of the stretchable, permeable and waterproof circuit

The fabrication of the multiple-layer circuits began with attaching Tegaderm to a quartz glass. After smoothly attaching the PI/Cu sheet on the Tegaderm, plasma cleaning was applied to clean the Cu foil. Then, photolithography was processed to pattern the circuit by a positive photoresist of AZ 4620. The photoresists were spin-coated on the Cu foil for 600 rpm of 10 s and 3000 rpm of 30 s, followed by baking for 5 min with a Tem of 110 °C. Next, the pattern was obtained by the photolithography and wet etching process. The left PI and photoresist were cleaned by the reactive ion etching and acetone. After obtaining the bottom layer, another layer of Tegaderm/Cu was adhered on the bottom layer, followed by the photolithography process to obtain another layer of Cu trace. As for the trace of connecting sensors, the PI/Cu trace was obtained by laser-cutting and then transfer-printed to the back side of the bottom layer of Tegaderm by water soluble tape and Sil-Poxy glue (just on the surface of Cu trace). Before that, Ag paste was filled into the patching holes for the later connecting between Cu trace and sensors. The connection between every circuit layer was also finished by filling Ag paste after laser-cutting connection holes. Then, a thin layer of Sil-Poxy was applied to encapsulate the Ag paste. Low-Tem solder joints bonded and electrically connected all the components. Finally, a layer of Tegaderm to be the encapsulation was covered on the top of all circuits.

### Fabrication of the stretchable biosensors

Firstly, the pre-stretched electrospinning SEBS film was deposited a layer of Cr (10 nm)/Au (100 nm) by sputtering. Then, the second layer of Cr/Au was obtained by the same way after releasing. The pattern SEBS electrode was gotten by laser-cutting methods. For the modification of working electrode of glucose sensor, a layer of Prussian blue was firstly electrodeposited on the electrode by cyclic voltammetry from 0 V to 0.5 V for 5 cycles in a mixed solution of 2.5 mM ferric chloride ($FeCl_3$), 100 mM potassium chloride (KCl), 2.5 mM Potassium ferricyanide ($K_3Fe(CN)_6$), and 100 mM hydrogen chloride (HCl). After that, a cocktail of 2 μL GOx (5 μ/μl), 1 μL bovine serum albumin (BSA, 2 mg/mL) and 2 μL glutaraldehyde (GA, 2%) are dipped on the electrode. After storage in the 4 °C refrigerator for overnight, 2 μL chitosan (2%) was dropped on the electrodes for immobilizing enzymes. The working electrode of the pH sensor was fabricated by electrodepositing $IrO_x$ on the SEBS electrode under a constant voltage of 0.7 V for 45 min. The electrodeposition electrolyte was firstly prepared by dissolving 300 mg iridium tetrachloride into 200 mL deionized (DI) water. This was followed by the addition of 2 mL hydrogen peroxide ($H_2O_2$) into the existing solution with continuous stirring. And then 1000 mg of oxalic acid dihydrate was added for stirring. Small quantities of anhydrous potassium carbonate were subsequently introduced to the continuously stirred solution to achieve a pH value of 10.5. Following the pH adjustment, the solution was stored at ambient room Tem for 48 h for stabilization. For the fabrication of the commonly used Ag/silver chloride (AgCl) reference electrode, the same sputtering process with Au electrode was operated. And then injecting 10 μL 0.1 M $FeCl_3$ on the electrode to get the Ag/AgCl electrode. Besides, there was another Au electrode to be the counter electrode of the glucose sensor. These electrodes were connected to the Cu traces by Ag paste with a thin layer of Sil-Poxy for encapsulation. The Tem sensor was achieved by the thermal resistor (NCP15WF104F03RC).

### In vitro study

The in vitro biocompatibility of different materials was evaluated by a live/dead kit assay using NIH/3T3 cells as model cells[53–55]. Briefly, samples were incubated with the culture medium overnight before co-culture with NIH 3T3 cells ($1 \times 10^4$ cells/cm$^2$). After different time points, cell viability was evaluated via the live/dead kit assay (Beyotime Biotechnology, Beijing, China), while cell proliferation was evaluated by CCK-8 assay (Beyotime Biotechnology, Beijing, China), both of which were performed following the manufacturer's manual. Cell scratch test and cell adhesion assessment were performed following previous reports[56,57].

Anti-bacterial performance was evaluated by the plate count method[58]. Briefly, samples were incubated with different bacteria suspension (i.e., *E. coli* (ATCC 25922) and *S. aureus* (ATCC 23235)) at the density of $1 \times 10^6$ CFU/mL for 6 h at 37 °C. Subsequently, the co-cultured suspension was extracted and spread onto the LB agar plates after dilution about 1000 times. After 24 h of culture, the colonies were recorded, and the anti-bacterial ability was evaluated using the formula: Anti-bacterial rate (%) = $(C_c\text{-}C_e)/C_c \times 100\%$, where $C_c$ and $C_e$ were the numbers of colonies in the control and experimental groups.

### In vivo study

Animal experiment was in accordance with the institutional guidelines and approved by the Research Committee of City University of Hong Kong. Sprague-Dawley (SD) male rats (about 8 weeks old, average weight 250–300 g) were used to establish a diabetic animal model by intraperitoneal injection of streptozotocin (~100 mg/kg for three consecutive days). After 2 weeks, SD rats with a glucose level greater than 16.7 mM were labeled as diabetic rats and used for subsequent experiments.

Then, rats were randomly divided into three groups and anesthetized via 3% isoflurane inhalation. Afterwards, four full-thickness round wounds of 12 mm in diameter were created on the dorsum, and then 10 μL prepared *E.coli* suspension ($1 \times 10^6$ CFU/mL) was added into the injured site using a pipette tip. Subsequently, different materials (i.e., S/G/P and iSAFE) were used to treat the wounds, and the wounds without any treatment were set as the control group. The wounds during the healing process were photographed to measure the injury size, and the closure rate was calculated as follows: Wound area (%) = $A_n/A_0 \times 100\%$, where $A_0$ indicates the wound areas on day 0, and $A_n$ represents the wound areas during the repair process. The wound areas are depicted and calculated by the software of ImageJ.

### Histological and immunochemical staining

H&E and MT staining analysis were performed on Day 6 and Day 14. The skin tissue samples were initially fixed by 10% formalin for 24 h, and the dehydrated and embedded in paraffin wax. After cutting and drying, the slides were rehydrated through a graded series of xylene, ethanol solutions, followed by a rinse in DI water. For H&E staining, hematoxylin, acting as the nuclear stain and an aqueous solution of eosin, functioning as the cytoplasmic stain, were applied to the slide,

respectively. After rapidly dehydrated and cleared through a graded ethanol series and xylene, slides were covered by the synthetic resin mounting medium and a coverslip. For MT staining, after deparaffinization and rehydration, the slides were submerged in Bouin's solution at room temperature for 60 min to enhance trichrome staining, followed by nuclear staining using Weigert's iron hematoxylin. Then, tissues were stained with Biebrich scarlet-acid fuchsin, treated with phosphomolybdic-phosphotungstic acid solution, followed by aniline blue staining. Subsequently, the slides underwent differentiation in 1% acetic acid and then transferred through graded alcohols, cleared in xylene, and mounted using a resinous medium. For immunochemical staining, the antigen retrieval process was firstly operated after deparaffinization and rehydration. Then, endogenous peroxidase activity was blocked by 3% hydrogen dioxide. After that, the primary antibody including CD68 (1:100, Servicebio, GB113109) and IL-6 (1:100, Servicebio, GB11117) were applied to the sections and incubated. Upon incubation with secondary antibody (Goat Anti-Rabbit IgG, Servicebio, GB23303), staining was developed using an appropriate substrate-chromogen. Finally, the slides were counterstained, dehydrated, cleared, and mounted. Slides were observed under an inverted microscope (Nikon Ti2-A). For immunofluorescence staining, similarly, after blocking the nonspecific binding sites using 5% goat serum (Biosharp), all tissue sections were incubated with different antibodies, including α-SMA (1:100, Servicebio, GB111364) and Ki-67 (1:100, Servicebio, GB111499), overnight at 4 °C before incubation with secondary antibodies (Cy3 conjugated Goat Anti-Rabbit IgG, Servicebio, GB21303). Then, all sections were washed with PBS and stained with DAPI (Servicebio) before observation with a confocal laser microscope (Leica TCS SP8 LIA FALCON, Leica Microsystems, Germany). Quantitative analysis of the stained images was conducted using ImageJ software.

### Transcriptome analysis

The RNA from tissue was extracted by TRIzol® Reagent based on its protocol. High-quality RNA samples were determined and quantified by the 5300 bioanalyzer (Agilent) and ND-2000 (NanoDrop Technologies). RNA purification, reverse transcription, library construction and sequencing were conducted by Shanghai Majorbio Biopharm Biotechnology Co., Ltd. For discovering the DEGs between two groups of samples, the expression magnitude of each transcript was ascertained by employing the methodology known as Transcripts Per Million reads (TPM). The functional enrichment analysis of GO and KEGG were executed to recognize the enrichment degree in both GO terms and metabolic pathways in comparison to the entire transcriptome background (with a Bonferroni-corrected $P$-value ≤ 0.05). The implementation of the GO functional enrichment and the KEGG pathway analysis were respectively achieved by Goatools and KOBAS[59].

### Clinical study

The clinical trial was in accordance with the institutional guidelines and approved by the Ethics Committee of the Chinese PLA General Hospital (Approval No. S2023-759-01). The genders of participants were not considered in the study design. All informed consents were obtained from the participants. All patients were measured during dressing changes by our sensors and commercial instruments, respectively. The data of our sensors was saved by smartphones and data from commercial instruments could be shown on their screen and recorded by us. The glucose concentration, pH value of wound exudate and temperature around the wound are calculated by the calibration curves shown in Fig. 4. For the six longitudinally monitored patients, we measured their wound exudates during their three or four treatments in the outpatient treatment room in two weeks. For the four single-detection patients, we just record one-time data of wound drainage fluids after surgery in the ward.

### Mechanical simulation (FEA)

In order to conduct a numerical analysis of the mechanical response and optimize the design parameters of various components within our electronic device, FEA was employed. The construction of three-dimensional (3D) models was initially carried out using SOLIDWORKS 2022, followed by meshing using MSC Apex 2022. All objects were meshed using linear hexahedron elements. To ensure convergence and accuracy, the mesh size was set to one-fifth of the width of the circuit. Subsequently, the mesh files were imported into Marc Mentat 2022 for the construction of the finite element model. Friction was neglected in the simulations. The simulation incorporated the following values for the elastic modulus ($E$) and Poisson's ratio ($\nu$): $E_{Cu}$ = 119 GPa and $\nu_{Cu}$ = 0.34 for copper; $E_{PI}$ = 0.8 MPa and $\nu_{PI}$ = 0.5 for PI.

### Molecular dynamics simulation

Molecular dynamics (MD) simulations of the Ag-TA-polymer (GelMA/SEBS) system were performed using the GROMACS 2021.5 package. TA, GelMA, SEBS and ethanol (EOH) were geometrically optimized by Gaussian 16 under density functional theory B3LYP/def2-SVP level with DFT-D3 dispersion correction and SMD (ethanol) implicit solvent model. Ambertools21 and ACPYPE were used to construct the general AMBER force field 2 (GAFF2) parameters, and Multiwfn was used to fit the restrained electrostatic potential 2 (RESP2) charge. Initial structure of Ag nanoparticle (4.6 nm in diameter) containing 2988 Ag atoms and corresponding INTERFACE force field parameters was obtained from the CHARMM-GUI website[60]. All simulation results were visualized by UCSF ChimeraX.

$12.1 \times 12.1 \times 16.5\ nm^3$ cubic box was established with an Ag nanoparticle, 12 TA and prebalanced polymer member (124 GelMA and 124 SEBS). The system was solvated in 16761 ethanol molecules, and energy minimization was performed by using the steepest descent algorithm with a force tolerance of 1000 kJ $mol^{-1}$ $nm^{-1}$. In all three directions, periodic boundary conditions were imposed. Then these systems were relaxed for 1 ns under NPT MD simulations, and position restraints with a constant of 1000 kJ $mol^{-1}nm^{-2}$ in three directions were performed on heavy atoms of the system except water. After completing the above steps, 200 ns NPT MD simulation with a timestep of 2 fs was performed. Pressure was maintained at 1 bar by the Parrinello-Rahman barostat in an isotropic manner, and Tem was maintained at 300 K by the V-rescal thermostat. The LINCS algorithm was performed to constrain the bond lengths of hydrogen atoms. Lennard-Jones interactions were calculated within a cutoff of 1.2 nm, and electrostatic interactions beyond 1.2 nm were treated with the particle-mesh Ewald (PME) method with a grid spacing of 0.16 nm.

### Correlation analysis

To assess the relationships between those measured biosensor parameters (i.e., glucose, pH, Tem) and WBS, we performed a pair-wise correlation analysis where Pearson's correlation coefficients were computed between all pairs of the key variables using the participant-specific longitudinal data. This analytic strategy took into account the individual heterogeneity and allowed for valid exploration of the correlation structure among the variables of interest. The R packages ggplot2 (version 3.4.2) and ggcorrplot (version 0.1.4.1) in the R (version 4.2.2) environment were used to visualize the correlation matrices.

### Hardware design

The main components of the circuit are as follows: MCU, energy harvesting and communication module, drug delivery actuation module, and physiological signal processing module. The power can be derived from the energy-harvesting function of the NFC when a smartphone is brought close to the iSAFE, allowing the entire circuit to be activated simultaneously. The drug delivery actuation module was achieved using an N-type MOSFET (BSS138BKVL, Nexperia) as a switch for

applying voltage to the channel to control the drug delivery. Measurements of glucose concentration, pH value, and temperature are associated with the potentiostatic method, open-circuit voltage (OCV), and voltage division methods, respectively. The potentiostat is a miniature and portable potentiostat in the three-electrode electrochemical system, which maintains a constant potential by controlling the electrode potential, enabling rapid detection of glucose potency. The potentiostat interface was constructed using a dual op-amplifier (AD8606, Analog Device) and a digital-to-analog converter (MCP47CVB12-E/MF, Microchip Technology). The dual op-amplifier was used to achieve the three-electrode system performance and current-to-voltage conversion. Meanwhile, the digital-to-analog convertered enables the DPV dynamic excitation signal to bias the reference and working electrodes. The analog signals from these circuits were then converted into digital signals through the ADC inside the MCU. When the sensor results were delivered from the MCU via the inter-integrated circuit, the NFC chip could transfer the data to the phone via RF interfaces.

### Characterization

All mechanical tests were tested by the Instron 5942 Miro Tester. SEM images were taken by the e-SEM (FEI Quanta 250). The resistance data was obtained by a data acquisition/multimeter system (DAQ6510, Keithley). The current and voltage responses of glucose and pH sensors were measured by the electrochemical station of CHI 660e. The impedance and phase of the NFC were measured by the impedance analyzer (E4990A, Keysight). The ELISA kits were bought from Shanghai Jianglai Industrial Limited By Share Ltd, and data were obtained by the MD SpectraMAX M5e Microplate Reader.

WVTR tests were conducted at 37.7 °C with a humidity of 67%. 40 mL DI water was placed into a 50 mL centrifuge tube with a diameter of 15 mm. The centrifuge tubes with water were sealed by different samples. The water mass losses were weighted after 12 h. The WVTR values were calculated by the mass losses dividing diameter and time.

In vitro degradation was examined by incubating samples in PBS solution with collagenase (3 μ/mL, Gibco, Hong Kong) at 37 °C for 14 days[58]. The degradation percentage was expressed as "Mass Loss (%) = $(W_1 - W_t)/W_1 \times 100\%$", where $W_1$ indicates the initial dry weights of different samples, while Wt represents the residual mass of samples at specific time intervals that was obtained by rinsing and freeze-drying. The equilibrium water sorption was assessed by immersing samples in PBS at 37 °C, and calculated based on the equation "water sorption (%) = $(W_s - W_0)/W_0 \times 100\%$", where $W_s$ is the weight of swollen samples at the equilibrated state, while $W_0$ is the initial dry weight. The tissue adhesion ability was evaluated lap-shear test and peel-off test following previously reported protocols[54]. Briefly, for lap-shear tests, glass slides coated with porcine gelatin were prepared, and then samples were positioned between two pieces of gelatin-coated glass slides with slight compression. Afterwards, the shear strength of the specimens was measured at a stretching speed of 3 mm/min and determined by dividing the maximum tensile force by the overlapping contact area. For peel-off tests, membrane samples were fixed to polyethylene terephthalate (PET) film and then attached to tissues by pressing (~ 2 N). Samples were pulled upward at a peeling angle of 90° and at a constant speed of 10 mm/min.

### Reporting summary

Further information on research design is available in the Nature Portfolio Reporting Summary linked to this article.

## Data availability

All data supporting the findings of this study are available within the article and its supplementary files. Any additional requests for information can be directed to and will be fulfilled by, the corresponding authors. Source data are provided in this paper.

## References


1. Yu, X. et al. Needle-shaped ultrathin piezoelectric microsystem for guided tissue targeting via mechanical sensing. *Nat. Biomed. Eng.* **2**, 165–172 (2018).
2. Song, E. et al. Miniaturized electromechanical devices for the characterization of the biomechanics of deep tissue. *Nat. Biomed. Eng.* **5**, 759–771 (2021).
3. Wang, C. et al. Monitoring of the central blood pressure waveform via a conformal ultrasonic device. *Nat. Biomed. Eng.* **2**, 687–695 (2018).
4. Zhang, B. et al. A three-dimensional liquid diode for soft, integrated permeable electronics. *Nature* **628**, 84–92 (2024).
5. Li, J. et al. Thin, soft, wearable system for continuous wireless monitoring of artery blood pressure. *Nat. Commun.* **14**, 5009 (2023).
6. Liu, Y. M. et al. Electronic skin as wireless human-machine interfaces for robotic VR. *Sci. Adv.* **8**, https://doi.org/10.1126/sciadv.abl6700 (2022).
7. Yu, X. et al. Skin-integrated wireless haptic interfaces for virtual and augmented reality. *Nature* **575**, 473–479 (2019).
8. Huang, Y. et al. A skin-integrated multimodal haptic interface for immersive tactile feedback. *Nat. Electron.* **6**, 1020–1031 (2023).
9. Li, D. et al. Touch IoT enabled by wireless self-sensing and haptic-reproducing electronic skin. *Sci. Adv.* **8**, eade2450 (2022).
10. Yao, K. M., et al. Encoding of tactile information in hand via skin-integrated wireless haptic interface. *Nat. Mach. Intell.* **4**, 893–903 (2022).
11. Li, J. et al. Wearable bio-adhesive metal detector array (BioMDA) for spinal implants. *Nat. Commun.* **15**, 7800 (2024).
12. Mannello, F., Ligi, D., Canale, M. & Raffetto, J. D. Omics profiles in chronic venous ulcer wound fluid: innovative applications for translational medicine. *Expert Rev. Mol. Diagn.* **14**, 737–762 (2014).
13. Brown, M. S., Ashley, B. & Koh, A. Wearable technology for chronic wound monitoring: Current dressings, advancements, and future prospects. *Front. Bioeng. Biotechnol.* **6**, 47 (2018).
14. Gao, Y. et al. A flexible multiplexed immunosensor for point-of-care in situ wound monitoring. *Sci. Adv.* **7**, https://doi.org/10.1126/sciadv.abg9614 (2021).
15. Gurtner, G. C., Werner, S., Barrandon, Y. & Longaker, M. T. Wound repair and regeneration. *Nature* **453**, 314–321 (2008).
16. Eming, S. A., Martin, P. & Tomic-Canic, M. Wound repair and regeneration: mechanisms, signaling, and translation. *Sci. Transl. Med.* **6**, 265sr266 (2014).
17. Shirzaei Sani, E. et al. A stretchable wireless wearable bioelectronic system for multiplexed monitoring and combination treatment of infected chronic wounds. *Sci. Adv.* **9**, eadf7388 (2023).
18. Power, G., Moore, Z. & O'Connor, T. Measurement of pH, exudate composition and temperature in wound healing: a systematic review. *J. Wound Care* **26**, 381–397 (2017).
19. Shukla, V., Shukla, D., Tiwary, S., Agrawal, S. & Rastogi, A. Evaluation of pH measurement as a method of wound assessment. *J. Wound Care* **16**, 291–294 (2007).
20. Li, J. Y. et al. Wearable and battery-free wound dressing system for wireless and early sepsis diagnosis. *Bioeng. Transl. Med.* https://doi.org/10.1002/btm2.10445 (2023).
21. Omar, A. S. et al. Association of time in blood glucose range with outcomes following cardiac surgery. *BMC Anesthesiol.* **15**, 14 (2015).
22. Swenne, C. L., Lindholm, C., Borowiec, J., Schnell, A. E. & Carlsson, M. Peri-operative glucose control and development of surgical wound infections in patients undergoing coronary artery bypass graft. *J. Hosp. Infect.* **61**, 201–212 (2005).

23. Jahan, I., George, E., Saxena, N. & Sen, S. Silver-nanoparticle-entrapped soft GelMA gels as prospective scaffolds for wound healing. *Acs Appl. Bio. Mater.* **2**, 1802–1814 (2019).
24. Yang, Z., Ren, X. & Liu, Y. Multifunctional 3D printed porous GelMA/xanthan gum based dressing with biofilm control and wound healing activity. *Mater. Sci. Eng. C. Mater. Biol. Appl.* **131**, 112493 (2021).
25. Kong, B. et al. Fiber reinforced GelMA hydrogel to induce the regeneration of corneal stroma. *Nat. Commun.* **11**, 1435 (2020).
26. Dong, J. C. et al. Ultra-highly stretchable and anisotropic SEBS/F127 fiber films equipped with an adaptive deformable carbon nanotube layer for dual-mode strain sensing. *J. Mater. Chem. A* **9**, 18294–18305 (2021).
27. Zhu, M. et al. Superstretchable electrode based on hierarchical assembly of triblock copolymer fiber membrane. *Chem. Eng. J.* **430**, https://doi.org/10.1016/j.cej.2021.132911 (2022).
28. Wu, T. et al. Tea eggs-inspired high-strength natural polymer hydrogels. *Bioact. Mater.* **6**, 2820–2828 (2021).
29. do Nascimento, M. F. et al. UV-polymerizable methacrylated gelatin (GelMA)-based hydrogel containing tannic acids for wound healing. *Drug Deliv. Transl. Res.* **13**, 3223–3238 (2023).
30. Chen, K. et al. An all-in-one Tannic acid-containing hydrogel adhesive with high toughness, notch insensitivity, self-healability, tailorable topography, and strong, instant, and on-demand underwater adhesion. *ACS Appl. Mater. Interfaces* **13**, 9748–9761 (2021).
31. Wang, X. et al. Robust but on-demand detachable wet tissue adhesive hydrogel enhanced with modified Tannic acid. *ACS Appl. Mater. Interfaces* **15**, 45676–45688 (2023).
32. Zhang, X., Reagan, M. R. & Kaplan, D. L. Electrospun silk biomaterial scaffolds for regenerative medicine. *Adv. Drug Deliv. Rev.* **61**, 988–1006 (2009).
33. Zhang, D. H. et al. Dealing with the foreign-body response to implanted biomaterials: Strategies and applications of new materials. *Adv. Funct. Mater.* **31**, https://doi.org/10.1002/adfm.202007226 (2021).
34. Amani, H., Alipour, M., Shahriari, E. & Taboas, J. M. Immunomodulatory biomaterials: Tailoring surface properties to mitigate foreign body reaction and enhance tissue regeneration. *Adv. Health. Mater.* **13**, e2401253 (2024).
35. Zhang, Q. et al. An anti-bacterial and anti-cancer fibrous membrane with multiple therapeutic effects for prevention of pancreatic cancer recurrence. *Biomater. Adv.* **137**, 212831 (2022).
36. Chung, H. J. et al. Stretchable, multiplexed pH sensors with demonstrations on rabbit and human hearts undergoing ischemia. *Adv. Health. Mater.* **3**, 59–68 (2014).
37. Huang, W. D., Cao, H., Deb, S., Chiao, M. & Chiao, J. C. A flexible pH sensor based on the iridium oxide sensing film. *Sens. Actuat A Phys.* **169**, 1–11 (2011).
38. Luong, J. H. T., Glennon, J. D., Gedanken, A. & Vashist, S. K. Achievement and assessment of direct electron transfer of glucose oxidase in electrochemical biosensing using carbon nanotubes, graphene, and their nanocomposites. *Microchim. Acta* **184**, 369–388 (2017).
39. Gao, W. et al. Fully integrated wearable sensor arrays for multiplexed in situ perspiration analysis. *Nature* **529**, 509–514 (2016).
40. Onda, M., Ariga, K. & Kunitake, T. Activity and stability of glucose oxidase in molecular films assembled alternately with polyions. *J. Biosci. Bioeng.* **87**, 69–75 (1999).
41. Khan, A. et al. Iontophoretic drug delivery: history and applications. *J. Appl. Pharm. Sci.* **1**, 11–24 (2011).
42. Zhu, Y. et al. A multifunctional pro-healing zwitterionic hydrogel for simultaneous optical monitoring of pH and glucose in diabetic wound treatment. *Adv. Funct. Mater.* **30**, 1905493 (2020).
43. Zhu, J. et al. Smart bioadhesives for wound healing and closure. *Bioact. Mater.* **19**, 360–375 (2023).
44. Martin, K. E. & Garcia, A. J. Macrophage phenotypes in tissue repair and the foreign body response: Implications for biomaterial-based regenerative medicine strategies. *Acta Biomater.* **133**, 4–16 (2021).
45. Cho, K. S. et al. Dendritic cells and M2 macrophage play an important role in suppression of Th2-mediated inflammation by adipose stem cells-derived extracellular vesicles. *Stem Cell Res.* **39**, 101500 (2019).
46. Lo Sicco, C. et al. Mesenchymal stem cell-derived extracellular vesicles as mediators of anti-inflammatory effects: Endorsement of macrophage polarization. *Stem Cell Transl. Med.* **6**, 1018–1028 (2017).
47. Nauroy, P. & Nystrom, A. Kallikreins: Essential epidermal messengers for regulation of the skin microenvironment during homeostasis, repair and disease. *Matrix Biol.* **6-7**, 100019 (2020).
48. Chen, C. J. et al. Single-cell RNA-seq analysis reveals cellular functional heterogeneity in dermis between fibrotic and regenerative wound healing fates. *Front. Immunol.* **13**, 875407 (2022).
49. Leon, C. et al. Transcriptomic analysis of a diabetic skin-humanized mouse model dissects molecular pathways underlying the delayed wound healing response. *Genes* **12**, 47 (2020).
50. Lawrence, T. The nuclear factor NF-kappaB pathway in inflammation. *Cold Spring Harb. Perspect. Biol.* **1**, a001651 (2009).
51. Gil, S. B. Implementing the triangle of wound assessment framework to transform the care pathway for diabetic foot ulcers. *J. Wound Care* **29**, 363–369 (2020).
52. Falanga, V., Saap, L. J. & Ozonoff, A. Wound bed score and its correlation with healing of chronic wounds. *Dermatol Ther.* **19**, 383–390 (2006).
53. Zhang, Q. et al. Micro- and nano-environment dual-modulated anti-tendon adhesion barrier membranes. *Mater Design* **219**, 110737 (2022).
54. Yang, Y. et al. Biomimetic, stiff, and adhesive periosteum with osteogenic-angiogenic coupling effect for bone regeneration. *Small* **17**, e2006598 (2021).
55. Yang, Y. et al. Photocrosslinkable nanocomposite ink for printing strong, biodegradable and bioactive bone graft. *Biomaterials* **263**, 120378 (2020).
56. Wu, H. B. et al. Stem cell self-triggered regulation and differentiation on polyvinylidene fluoride electrospun nanofibers. *Adv. Funct. Mater.* **34**, 2309270 (2024).
57. Shi, S. et al. A skin-like nanostructured membrane for advanced wound dressing. *Compos. Part B Eng.* **250**, 110438 (2023).
58. Zhang, Q. et al. A biomimetic adhesive and robust jJanus patch with anti-oxidative, anti-inflammatory, and anti-bacterial activities for tendon repair. *ACS Nano* **17**, 16798–16816 (2023).
59. Xie, C. et al. KOBAS 2.0: a web server for annotation and identification of enriched pathways and diseases. *Nucleic Acids Res.* **39**, W316–W322 (2011).
60. Choi, Y. K. et al. CHARMM-GUI Nanomaterial modeler for modeling and simulation of nanomaterial systems. *J. Chem. Theory Comput.* **18**, 479–493 (2022).


## Acknowledgements

This work was supported by the National Key Research and Development Program of China (grant no. 2022YFB3205600), National Natural Science Foundation of China (grant no. 62122002), City University of Hong Kong (grant nos. 9667221, 9678274 and 9610444), as part of the InnoHK Project 2.2–AI-based 3D ultrasound imaging algorithm at Hong Kong Center for Cerebro-cardiovascular Health Engineering (COCHE), the Research Grants Council of the Hong Kong Special Administrative Region (grants nos. RFS2324-1S03, 11213721, 11215722, 11211523), Shenzhen Science and Technology Innovation Commission (grant no. SGDX20220530111401011), Innovation and Technology Commission of Hong Kong SAR Government (grant no. MRP020/21), Beijing Natural Science Foundation (grant no. 7232146).

## Author contributions

X.Y. and X.H. conceived the idea and designed the projects. X.H., Q. Z., and X.Y. wrote the manuscript. X.H. designed the whole system and conducted overall experiments. X.H. and Q.Z. designed the BEWI and device integration. Y.Y. designed the circuits. L.C. and X.H. conducted the mechanical modeling and schematic design. Q.Z., X.H., J.M., Z.L., J.S., G.G., Xx.H., J.W., Y.J., Z.G., J.L., Y.C., J.Z., C.Y., and J.L. conducted the material, cell and animal characterizations and analyzed the experimental data. P.W., K.Y., Y.L., D.L., B.Z., H.C., Y.H., Y.H., and Z.C. assisted in the fabrication and testing experiments. X.Y., X.T., X.M., H.L., R.Y., B.F., and K.R. evaluated the experiments and managed the projects.

## Competing interests

The authors declare no competing interests.

## Additional information

**Supplementary information** The online version contains supplementary material available at https://doi.org/10.1038/s41467-025-61261-8.

**Correspondence** and requests for materials should be addressed to Rungong Yang, Heng Li, Xiaoming Tao, Xiaohui Ma or Xinge Yu.

**Peer review information** *Nature Communications* thanks Huanyu Cheng, Wei Gao, and the other anonymous reviewer(s) for their contribution to the peer review of this work. A peer review file is available.



[1]Department of Biomedical Engineering, City University of Hong Kong, Kowloon, Hong Kong, China. [2]Institute of Digital Medicine, City University of Hong Kong, Kowloon, Hong Kong, China. [3]Department of Building and Real Estate, The Hong Kong Polytechnic University, Kowloon, Hong Kong, China. [4]School of Public Health, LKS Faculty of Medicine, The University of Hong Kong, Kowloon, Hong Kong, China. [5]Department of Civil and Environmental Engineering, The Hong Kong Polytechnic University, Kowloon, Hong Kong, China. [6]Department of Chemistry, Hong Kong Baptist University, Kowloon, Hong Kong, China. [7]Hong Kong Center for Cerebra-Cardiovascular Health Engineering, Hong Kong Science Park, New Territories, Kowloon, Hong Kong, China. [8]School of Biomedical Engineering, Shenzhen Campus of Sun Yat-sen University, Shenzhen, PR China. [9]Department of Emergency Medicine, West China Hospital, Sichuan University/West China School of Nursing, Sichuan University, Chengdu, China. [10]Disaster Medical Center, Sichuan University, Chengdu, China. [11]Nursing Key Laboratory of Sichuan Province, Chengdu, China. [12]Macao Institute of Materials Science and Engineering (MIMSE), Faculty of Innovation Engineering, Macau University of Science and Technology, Taipa, Macao. [13]School of Pharmacy, Shenzhen University Medical School, Shenzhen University, Shenzhen, China. [14]Institute of Fiber Materials and Devices, Fudan University, Shanghai, China. [15]Research Institute for Intelligent Wearable Systems, The Hong Kong Polytechnic University, Kowloon, Hong Kong, China. [16]School of Fashion and Textiles, The Hong Kong Polytechnic University, Kowloon, Hong Kong, China. [17]Department of tissue repair and regeneration, The first medical center of Chinese PLA General Hospital, Beijing, China. [18]Department of vascular and endovascular surgery, The first medical center of Chinese PLA General Hospital, Beijing, China. [19]City University of Hong Kong Shenzhen Research Institute, City University of Hong Kong, Shenzhen, China. [20]These authors contributed equally: Xingcan Huang, Qiang Zhang, Yawen Yang, Lung Chow, Jie Ma. ✉e-mail: yangrungong@139.com; heng.li@polyu.edu.hk; xiao-ming.tao@polyu.edu.hk; maxiaohui@301hospital.com.cn; xingeyu@cityu.edu.hk